Journal Pre-proof

Preferentially-orientated gradient precipitates enable unique strength-ductility synergy in Mg-Sn binary alloys

Lutong Zhou , Yong Sun , Guodong Zou , Haidong Hu , Yanhui Zhang , Huhu Su , Shijian Zheng , Yulong Zhu , Peng Chen , Carlos Fernandez , Qiuming Peng

PII: S1005-0302(25)00346-9
DOI: https://doi.org/10.1016/j.jmst.2025.01.082
Reference: JMST 6573

To appear in: *Journal of Materials Science & Technology*

Received date: 8 December 2024
Revised date: 19 January 2025
Accepted date: 27 January 2025

Please cite this article as: Lutong Zhou , Yong Sun , Guodong Zou , Haidong Hu , Yanhui Zhang , Huhu Su , Shijian Zheng , Yulong Zhu , Peng Chen , Carlos Fernandez , Qiuming Peng , Preferentially-orientated gradient precipitates enable unique strength-ductility synergy in Mg-Sn binary alloys, *Journal of Materials Science & Technology* (2025), doi: https://doi.org/10.1016/j.jmst.2025.01.082

Highlight

- A unique preferentially-orientated gradient structure is firstly found in UPJTed Mg alloys
- A strength-ductility synergy (341 MPa, 15 %) is achieved in UPJTed Mg-Sn alloys
- The formation reasons of gradient precipitate structure have been clarified.
- The strengthening role is related to fine particles with Orowan strengthening.
- The ductility reason lies in coarse particles with good plastic/shear deformation.

Research Article

Preferentially-orientated gradient precipitates enable unique strength-ductility synergy in Mg-Sn binary alloys

Lutong Zhou [a], Yong Sun [a,*], Guodong Zou [a], Haidong Hu [a], Yanhui Zhang [a], Huhu Su [b], Shijian Zheng [b], Yulong Zhu [c], Peng Chen [c], Carlos Fernandez [d], Qiuming Peng [a,*]

[a] State Key Laboratory of Metastable Materials Science and Technology, Yanshan University, Qinhuangdao 066004, China

[b] School of Materials Science and Engineering, Hebei University of Technology, Tianjin 300401, China

[c] Key Laboratory of Automobile Materials of Ministry of Education & School of Materials Science and Engineering, Jilin University, Changchun 130025, China

[d] School of Pharmacy and Life Sciences, Robert Gordon University, Aberdeen AB107GJ, United Kingdom

[*]Corresponding authors.

E-mail addresses: sunyong@ysu.edu.cn (Y. Sun), pengqiuming@ysu.edu.cn (Q. Peng).

Abstract

Conventional manufacturing approaches, including casting, thermal deformation and annealing, have faced great challenges in achieving both exceptional strength and ductility for Mg alloys. Herein, we report an effective strategy for simultaneously enhancing the tensile yield strength (YS = 341 ± 9.6 MPa) and elongation (EL = 15% ± 1%) of a Mg-4Sn (at.%) binary alloy at room temperature, which has been prepared by an ultrahigh-pressure treatment

followed by Joule-heat treatment (UPJT). More attractively, the aging condition (80 μs, 500 Hz, 600 s) is the most time-efficient mode for aged Mg alloys. The reason is mainly associated with the presence of a unique preferentially-orientated gradient precipitate structure, as confirmed by transmission electron microscopy observations, density functional theory calculations and molecular dynamics simulations. Both experimental and theoretical results demonstrate that twin boundary-induced precipitation followed by precipitate-assisted twin boundary migration accounts for the formation of gradient precipitate structures. The fine Mg_2Sn particles can effectively pin dislocation movement to enhance its strength. Comparatively, the coarse Mg_2Sn particles can undergo plastic deformation and shear deformation, contributing to its high ductility. The strategy of preferentially orientated gradient structure provides a budding perspective for designing new Mg alloys with superior mechanical properties.

Keywords: Joule-heat treatment; High-resolution TEM; Molecular dynamics; Density functional theory

1. Introduction

The growing concerns regarding dual-carbon targets have inspired us to develop novel high-performance Mg alloys in recent years, which exhibit significant potential for energy conservation in aircraft and automobiles due to their distinct advantages of low density, high specific strength and good castability [1]. However, compared to Al alloys or steels, two critical bottlenecks related to low strength and poor ductility have severely limited their wide application [2]. The strength has greatly improved in the past decades in light of alloying, grain refinement, composites manufacturing, texture engineering, and thermal-mechanical treatment

[3-5]. Unfortunately, the increase in strength is usually accompanied by a sacrifice of its ductility to some extent. In this regard, improving strength and ductility of Mg alloys simultaneously is of significant importance but a grand challenge so far.

Unlike strength, the ductility in Mg alloys is mainly associated with their intrinsic structure. Basically, as an HCP-type structure, Mg lacks adequate slip systems to fulfill the von-Mises criterion for homogeneous plastic deformation [6]. Simultaneously, due to its low crystal symmetry, strain accommodation along the *a*-axis is strongly preferred, making it difficult to activate slip deformation along the *c*-axis. Therefore, the activation of twinning is the main mode for coordinating deformation at low temperatures. Subsequently, it is prone to generate strong crystallographic textures during deformation [7]. Therefore, two methods related to twinning and microalloying have been developed to improve the ductility of Mg alloys. On the one hand, twinning provides an alternative shear mechanism that accommodates plastic deformation along the *c*-axis [8], contributing to good mechanical properties. However, the high density twins are unable to provide a high strength due to the high mobility of twin boundary (TB) under strain, leading to twin thickening or coalescence [9]. On the other hand, microalloying, especially the addition of rare earth (RE) elements, is an effective path for altering texture and enhancing ductility [10]. However, improving them through heat treatment and achieving high strength levels is usually difficult due to the low alloying composition [11]. In this regard, the key issue is to overcome the strength-ductility trade-off dilemma in Mg alloys to achieve strength-ductility synergy.

Theoretically, aging precipitates with a high volume fraction that exhibit exceptional lattice matching with the matrix can enhance both strength and ductility through pinning

dislocations and coordinating deformations [12]. Nevertheless, due to the significant differences in lattice constants between the HCP matrices and precipitates, preparing a dense matching interface between aged precipitates and matrix has become a technical challenge in the field of Mg alloys. Therefore, applying an external field, such as an electric field, during the aging process might be one of the effective methods for achieving good lattice matching between the strengthening particles and the matrix. For example, a highly oriented Cu_3Sn precipitate can be prepared along a low-resistance path of electron movement under a Joule-heat treatment (JT) [13]. Furthermore, considering the operating conditions of the JT process at low temperatures, high supersaturated solid solubility related to aging kinetics can aid in the acquisition of large volume fractions of strengthening phases with appropriate lattice-matching interfaces. Mg-Sn-based alloys are considered promising age-hardenable Mg alloys due to the high solubility of Sn (3.35 at.% at 561 °C) and their significantly reduced solubility in Mg matrix at room temperature [14]. Although RE elements also exhibit high solid solubility in the Mg matrix and Mg-RE-based alloys usually exhibit remarkable age-hardening responses and promising YS levels of 400 MPa [15]. However, the high cost and resource scarcity make the abundant usage of RE elements as the major solute additions unacceptable in commercial applications [16].

Recently, we have confirmed that the ultrahigh-pressure (UP) technique is an effective method for tailoring the microstructure of Mg alloys, particularly in promoting twin formation [17, 18] and phase transformation [19], similar to the effects of chemical composition and temperature. Compared with traditional heat treatment, it has at least one significant feature: increasing solubility. A few years ago, we successfully extended the solid solubility limitation

of Al alloying element (~25 at.%) in Mg alloys, resulting in a unique solid-solution strengthening and age-hardening response [20]. Herein, a model of Mg-4Sn (at.%) alloy was involved to test the possible strength-ductility synergy role dependent on aging precipitate interface modification. An industrial process with a UP treatment (4 GPa, 800 °C) was performed to prepare single-phase Mg alloys, suggesting its highest aging driving force. Subsequently, a JT process at room temperature has been performed. A distinctive strength-ductility synergy phenomenon was detected, which is mainly associated with the formation of preferentially-orientated gradient Mg_2Sn structures. In addition, the underlying mechanisms related to the impacts of pulse current on the aging response and crystallography characteristics of precipitates in Mg alloys was clarified. Both formation reason and strength-ductility synergistic mechanism of preferentially-orientated gradient Mg_2Sn structure were investigated based on experimental observations in combination with theoretical analyses.

2. Material and methods

2.1. Sample preparation

The Mg-4Sn (at.%) alloy ingot was produced by induction melting using a steel crucible under the protection of an argon atmosphere, and then cast into a steel mold. The cast alloy was homogenized at 400 °C for 6 h and cooled in the furnace. Then, the homogenized sample was machined into cylindrical specimens with a diameter of 10 mm and a length of 14 mm for UP treatment in a modified CS-IB type hexahedral anvil apparatus. The sample was wrapped with tantalum foil and inserted in a boron nitride capsule. The hydrostatic pressure was obtained by the press along three axes. The samples were treated for 30 min at temperatures from 600 to

1100 °C under UP treatment under 4 GPa. The heating rate and time to boost pressure were 6 °C/s and 2 min, respectively. After UP treatment, the samples were cooled to room temperature by circulating water before unloading pressure. Theoretically, the Clausius-Clapeyron equation shows the relationship between the slope of the temperature pressure change of the phase and the molar latent heat and the changed volume of the phase transition. Since the volume of magnesium alloy expands and the molar latent heat is positive during melting, the slope of temperature and pressure change is positive. Therefore, heat treatment beyond the melting point of magnesium alloys under high pressure is possible. Experimentally, this phenomenon that the melting point of the alloy increases under high-pressure conditions has been confirmed in our previous articles [17, 18]. The UP-treated sample was subjected to aging heat treatment in a silicone oil bath at 200 °C, which was denoted as UPA. As a comparison, the cast alloys underwent solid solution treatment at 500 °C for 8 h, followed by aging heat treatment in a 200 °C silicone oil bath, denoted as T6.

The UP-treated sample was machined into sheet specimens with the dimensions of 13 mm × 7 mm × 2 mm, and then the oxide was removed from the surface using the SiC paper. The sheet was connected to a direct current pulse power supply through Cu wires. The JT experiment was conducted at a current density of 4.5×10^3 A/cm^2, with a voltage of 100 V, a pulse width of 80 μs and a frequency of 500 Hz. The sample was recorded by quenching every 60 s. The duty cycle is one of the main factors influencing the heat generation of the sample. Considering systematic errors, the duty cycle has been calculated to be 3%–5% in this work. Moreover, during the JT experiment, fans were utilized for supplementary air cooling, while the temperature was monitored using an infrared thermometer and maintained at about 50 °C.

The JTed sample after a UPed treatment under 4 GPa at 800 °C was denoted as an ultrahigh-pressure treatment followed by Joule-heat treated (UPJTed). The as-cast and as-UPed samples were involved as references.

2.2. Mechanical properties

Microhardness was measured by an FM-ARS-9000 Vickers hardness tester. The load and the dwelling time were 100 g and 15 s, respectively. The average hardness has been calculated using the dependence of 5 × 5 matrix measures. Tensile tests were performed at room temperature (RT) using a WDW-DDL 550 universal material testing machine at a normal strain rate of 1×10^{-3} s^{-1}. The dog bone-shaped tensile samples had a gauge length of 8 mm, a width of 2 mm and a thickness of 2 mm. The value was averaged over at least three parallel samples.

2.3. Microstructural characterization

The microstructural investigations were performed using an optical microscope (OM) and scanning electron microscope (SEM), where the samples were prepared by a procedure involving grinding up to 2000 SiC paper, followed by mechanical polishing with 9, 3 and 1 μm water-free diamond suspensions and finally polished using 0.05 μm colloidal silica. The final step included chemical polishing in a fresh solution containing a mixture of 100 mL alcohol and 5 mL nitric acid. For electron backscattering diffraction (EBSD) examinations, the UPJTed samples were prepared by a procedure involving mechanically grinding up to 5000 SiC paper. Ensure there are no visible scratches on the surface. Then, the UPJTed samples were polished on a polishing machine using a water-free diamond suspension with a particle size of 1 μm. Finally, the UPJTed samples were electrochemically polished in an AC2 electrolyte at 20 V for

90 s and at −30 °C. EBSD was conducted using the JEOL JSM-7800 equipped with an HKL-EBSD system. The acceleration voltage during data acquisition is 20 kV, the beam spot intensity is 70, the working distance is 15 mm, and the sample inclination is 70°. The EBSD results were analyzed by the Channel 5 software. The misorientation angles between the adjacent grains are used to identify the low angular grain boundary (LAGB, $2° \leq \theta \leq 15°$) and high angular grain boundary (HAGB, $\theta \geq 15°$), as indicated by green and black lines, respectively. The average grain sizes were estimated from the inverse pole figure (IPF) maps by using the major axis of fitted ellipse (with the software of Channel 5).

The microstructure of the deformation characteristics was mainly characterized by Talos-F200 transmission electron microscope (TEM) and JEM-ARM300F aberration-corrected scanning TEM (STEM) operated at a voltage of 300 kV. Specimens for TEM observation were extracted from the UPJTed samples. Firstly, the UPJTed sample was machined into sheets with a thickness of ~0.8 mm, and subsequently thinned using mechanical grinding to 30 μm. Then, the specimens were prepared by ion-milling (PIPS II System) under −30 °C. The specific process parameters are as follows: deflection ±10° milling for 10 min at 5 keV, deflection ±7° milling for 30 min at 4.5 keV ,and deflection ±3° milling for 30 min at 3.5 keV. Finally, all TEM samples were cleaned by Solarus II Plasma Cleaner. The sizes of precipitates were calculated by Image Pro Plus software. Multiple TEM images were selected from the UPJTed sample for statistics and averaging. The average size of coarse and fine particles was calculated based on 100 random dots. The length and width of the particles were calculated separately. The coarse and fine particles correspond to the particles in the matrix and in the interior of refined bands, respectively.

2.4. DFT calculations

The Density Functional Theory (DFT) calculations were carried out by the projected augmented wave method (PAW) as implemented in the Vienna Ab-initio Simulation Package (VASP) [21, 22]. The Perdew-Burke-Ernzerhof (PBE) function [23] under the generalized gradient approximation (GGA) [24] was adopted to describe the exchange-correlation energy. The electron wave function was expanded by the plane wave basis set with a kinetic energy cut-off of 300 eV. The supercell models of bulk Mg, $[10\bar{1}2]$ twin, and $[10\bar{1}2]$ step were separately optimized by using the conjugate gradient algorithm with an energy convergence threshold of 10^{-6} eV/atom, and a force criterion of 0.05 eV/Å. The *k*-point meshes were 5 × 3 × 3, 3 × 3 × 7, and 3 × 5 × 5, respectively, were applied for the Brillouin zone integration. The visualization of the electron localization function was performed by the VESTA package [25].

In addition, the calculation of vacancy formation energies and their diffusion energy barriers was also performed by DFT. The modified embedded atom method (MEAM) potential of Mg from Kim [26] was adopted to describe the atomic interactions. A time step of 1 fs was used in accordance with the Verlet integration method. Vacancy formation energies can be calculated using the following equation:

$$E_{\mathrm{f}} = E_{(n-1)} - (n - 1/n)E_{(n)} \quad (1)$$

where $E_{(n-1)}$ was the energy of the system with a single vacancy, $E_{(n)}$ and n were separately the energy and the total number of atoms in the parent lattices of hcp Mg, $\{10\bar{1}2\}$ twin and $\{10\bar{1}2\}$ step. The Nudged Elastic Band (NEB) method [27] was applied to search the saddle point along possible migration paths, thereby the energy barriers of vacancy diffusions can be derived.

2.5. MD simulations

The interactions of Mg_2Sn precipitates and TBs were performed using LAMMPS, in which the MEAM interatomic potential for the Mg-Sn binary system developed by Kim et al. [28] was used. The common neighbor analysis (CNA) [29] algorithm implemented in the open visualization tool (OVITO*)* [30] was used to identify the local crystal structure. Simulation models were first equilibrated with a conjugate gradient method, following the relaxation under ensemble for 20 ps. Then, a shear strain was applied at an engineering shear strain rate of 5×10^8 s^{-1}. The simulation temperature was 100 K to reduce thermal noise. The simulation models satisfy the orientation relationship (OR), i.e., $(0001)_{\mathrm{Mg}} \,||\, (110)_{\mathrm{Mg_2Sn}}$, $[11\bar{2}0]_{\mathrm{Mg}} \,||\, [001]_{\mathrm{Mg_2Sn}}$. For the twin-precipitate simulation, the dimension of the simulation system was 48 nm× 22 nm× 15 nm, and periodic boundary conditions were applied along the *x* and *z* directions. A $\{10\bar{1}2\}$ extension twin was pre-planted in the matrix and the space between the TBs was ~15 nm. Subsequently, the Mg_2Sn precipitate with the dimensions of 3 nm × 3 nm × 3 nm was introduced at the TB to mimic the pinning of the TB observed in experiments. Also, the precipitates were also embedded near the TB to mimic that the TB was approaching the precipitates.

3. Results

3.1. Mechanical properties and microstructure characteristics

Fig. 1(a) shows the hardness variations of the Mg-4Sn samples treated under different conditions. Noticeably, the UPJTed Mg-4Sn sample shows a typical "volcanic" trend. During JT, the hardness value initially remains stable and subsequently increases sharply to reach a

peak hardness of 88.7 HV at 600 s, which is approximately 1.37 times and 1.07 times higher than those of the T6 and UPAed samples, respectively. More importantly, the time required for the UPJTed Mg-4Sn sample to reach the peak hardness is merely 1/144 that of the UPAed Mg-4Sn sample. Fig. 1(b) shows the representative true stress-strain tensile curves of Mg-4Sn alloys in different states at room temperature. The YS of the UPJTed Mg-4Sn sample is 341.1 ± 9.6 MPa, which is 3.6 and 4.09 times greater than those of the as-cast and UPed Mg-4Sn samples, respectively (Table 1). Interestingly, the EL of the UPJTed Mg-4Sn sample is approximately 15 %, which is 4.05 times greater than that of the UPAed Mg-4Sn sample. As summarized in Fig. 1(c), the comprehensive performance overwhelms those of aged Mg-Sn-based alloys and conventional T6 state Mg-RE-based alloys [31-42]. Attractively, it exhibits an outstanding aging peak response (ambient temperature, 600 s) (Fig. 1(d)), which is significantly better than other aged peak alloys [4, 32, 36, 39-47].

Fig. 2(a) shows the hardness variation of UPed Mg-4Sn samples treated under different conditions. Specifically, the hardness values exhibit two typical characteristics. On the one hand, a representative “V-shaped” trend is observed under a constant pressure of 4 GPa during the whole temperature range. The hardness value of the as-cast sample is about 64 HV, which is remarkably reduced with increasing UPed temperature. The lowest value of 60 HV is attained for the UPed 800 Mg-4Sn sample. Subsequently, the values are increased with further increasing the UPed temperature. According to the optical observations (Fig. 2(b–e)), a typical UPed solid solution is confirmed at 800 °C at 4 GPa, as evidenced by the elimination of precipitates in combination with the appearance of equiaxed grains with a size of 330 μm. When the temperature exceeds 800 °C, the presence of a remelting sphere in UPed Mg-4Sn

alloys indicates that the alloy commences to overheat at this heat treatment temperature. It is noteworthy that a typical dendrite microstructure is observed at a temperature of 1100 °C, indicating the occurrence of re-solidification during this process [48], in which its dendrite spacing is clearly lower than that of the as-cast sample. To attain a high volume fraction of the strengthening phase, the UPed 800 Mg-4Sn solid solution is selected for JT at different time intervals. To highlight the structural features more intuitively, we employ the peak-aged UPJTed Mg-4Sn sample (600 s) for SEM characterization. The results in Fig. 2(f, g) demonstrate the presence of a high volume fraction of precipitates and several oval-shaped twins with various orientations during the JT process. Specifically, the precipitates exhibit unidirectional growth within one grain. Simultaneously, the precipitate bands are observed near the twin boundary, as indicated by yellow arrows. The X-ray diffraction (XRD) patterns of Mg-4Sn alloy are displayed in Fig. 2(h, i). Based on the XRD analysis, the major phases of the alloys present in different conditions are α-Mg matrix and β-Mg_2Sn phase, confirming that the remelting spheres shown in Fig. 2(d) and the unidirectional growth particles presented in Fig. 2(g) are Mg_2Sn phases. Furthermore, the result indicates that the novel JT process does not induce new phase transformation in this study.

3.2. Preferential-orientated gradient precipitates

As evidenced by the bright-field (BF) TEM image (Fig. 3(a)), a high number density of Mg_2Sn particles is oriented along three directions in the UPAed Mg-4Sn sample. Moreover, the selected area electron diffraction (SAED) pattern parallel to $[0001]_\alpha$ indicates that Mg_2Sn particles (represented by β) are formed on the basal planes and grow along three $[11\bar{2}0]$ directions at an angle of 120°. The OR between the matrix and Mg_2Sn is $[0001]_\alpha$ // $[111]_\beta$,

$(11\bar{2}0)_\alpha$ // $(110)_\beta$. In contrast, as confirmed by the TEM image (Fig. 3(b)), the majority of particles are obviously growing in the same direction in the matrix of the UPJTed Mg-4Sn alloy in the matrix, which is quite different from the UPAed Mg-4Sn samples (Fig. 3(a)) and other traditional T6 aged Mg-Sn alloys [41]. Obviously, two particles with different dimensions are detected in the UPJTed Mg-4Sn alloy. The average particle lengths based on 100 randomly selected particles in the matrix are approximately 216 nm for large particles and 33.8 nm for fine particles (Fig. 3(c)). Specifically, the large particles nucleate on the basal plane and grow along the $[11\bar{2}0]$ direction (Fig. 3(d)), exhibiting a crystallization OR of $[11\bar{2}0]_\alpha$ // $[100]_\beta$, $(0002)_\alpha$ and $(10\bar{1}0)_\alpha$ // $\{220\}_\beta$. The energy dispersive spectroscopy (EDS) results (Fig. 3(e–g)) show the presence of Sn enrichment in the particle, which is consistent with the detection of the Mg_2Sn phase by XRD. The interface atomic structure indicates an OR of $(0002)_\alpha$ // $(220)_\beta$ and a semi-coherent matching relationship with a mismatch of approximately 4.5%, as proven by the atomic-resolution high-angle annular dark field (HAADF) STEM images taken with the electron beam aligned along the $[11\bar{2}0]_\alpha$ direction (Fig. 3(h)). In addition, the high resolution TEM (HRTEM) image and the SAED pattern (Fig. 3(i)) corresponding to the white dotted box indicated by Fig. 3(b) demonstrate that the fine Mg_2Sn particles exhibit the same OR as those of larger particles within the matrix.

3.3. Refining precipitate bands

It is displayed in Fig. 3(b) that the fine precipitates are mainly located in the refined areas and TB. As exhibited in the HRTEM image of the UPJTed sample (Fig. 4(a)), it is clearly confirmed that the plane of $(0001)_M$ and $(0001)_T$ is rotated 86.3° to overlap in the $<11\bar{2}0>$ zone axes, suggesting the presence of $\{10\bar{1}2\}$ tension twins. Specifically, there are three typical

characteristics related to twin interfaces. Firstly, there are significant increases in the density of basal-prismatic (BP) facets in the $\{10\bar{1}2\}$ twin interface, which are greatly different from the commonly deformed $\{10\bar{1}2\}$ twin interfaces. Secondly, some nanoscale Mg_2Sn particles are segregated in TBs. Moreover, the {220} plane of the Mg_2Sn particle is parallel to the (0002) and $(10\bar{1}0)$ planes of the matrix, maintaining consistency in orientation with the other particles nucleated in the matrix. Finally, the (220) plane of the particles is approximately parallel to the (0002) and $(10\bar{1}0)$ planes within the twin. The deflection angle between them is about 3.7°.

Near-situ TEM observation was employed to investigate the structural evolution of UPed800Mg-4Sn samples (Fig. 4(b)) during the JT process. It is noted that the UPed800Mg-4Sn samples (Fig. 4(b, c)) exhibit no discernible defects such as dislocations, SFs, or twins in experimental observations. Firstly, a high density of dislocations and stacking faults (SFs) are observed in the matrix (Fig. 4(d)), which is associated with electro-work hardening resulting from the athermal electromigration effect [49]. Specifically, the electron wind force, acting as the driving force for the accumulation of lattice strain, continuously imposes on the Mg lattices, promoting the generation of dislocations and SFs [50]. Subsequently, the sample (Fig. 4(e)) exhibits dislocation entanglement within the matrix, representing localized stress concentration and also serving as the initiation site for twin nucleation. Under the persistent influence of the electron wind force, twin nucleation occurs at the sites of stress concentration, as depicted in Fig. 4(f). The SAED pattern (Fig. 4(g)) confirms that the twin structure corresponds to a $\{10\bar{1}2\}$ tensile twin. Simultaneously, in a locally magnified HAADF-STEM atomic resolution image (Fig. 4(h)), the nucleation of nanoscale Mg_2Sn particles with crystallographic orientation is was observed, consistent with that shown in Fig. 4(a).

Additionally, the EDS analysis corresponding to the HAADF-STEM image shows the segregation of Sn atoms, which is similar to the atom segregation in deformed TBs reported by Nie et al. [51]. With the continuous enrichment of Sn atoms, several nanoscale particles are preferentially formed at the TBs (Fig. 4(i)). Finally, a large number of the particles are detected in the TBs (Fig. 4(j)), but there is no obvious increase in particle size. Furthermore, a typical gradient structure has been observed, with the fine particles mainly segregated near the TBs and the large particles distributed in the matrix. Therefore, the formation process of unique refined structure is described as follows: Supersaturated solid solution (SSSS) → dislocation entanglement → twin nucleation → particle segregation → refined structure.

4. Discussion

4.1. Effect of pressure on aging kinetics and thermodynamics

Rapid aging kinetics plays a crucial role in the industrial application of Mg alloys. Although Mg-Sn binary alloys are promising age-hardenable metal materials, their aging kinetics is still unsatisfactory because it generally takes more than 300 h to reach the peak hardness [41]. To enhance the aging response, we selected Mg-4Sn alloy for T6 treatment, which is higher than the atmospheric pressure solid solubility limit (3.35 at.%). However, as depicted in Fig. 1(a), it is evident that the alloy requires more than 100 h to reach peak hardness. This indicates that the increment of solid solubility does not serve as a method to significantly improve the aging kinetics of Mg-Sn alloy. Comparatively, the recent results exhibit that high-pressure technique can offer a wide range of potential approaches to control the crystal structure, chemical composition, and microstructure of materials [52]. Theoretically,

the Clausius-Clapeyron equation describes the relationship between the slope of temperature-pressure (*T*-*P*) changes of the phase and the molar latent heat and volume variation during the phase transition. The Clausius-Clapeyron equation can be described as follows [53]:

$$\mathrm{d}T/\mathrm{d}P = T_{\mathrm{m}}(V_2 - V_1)/LV_1 \quad (2)$$

where T_{m} is the melting point under atmospheric pressure, V_1 and V_2 are the molar volumes of solid and liquid states, respectively, and L is the molar latent heat ($L > 0$). Due to the volume expansion of Mg alloy during melting, (V_2−V_1) is positive. Therefore, it can be seen from the above equation that the slope of temperature and pressure changes is positive. Namely, the melting point of Mg alloy increases as the pressure is increased.

Generally, nucleation of precipitates can be divided into uniform nucleation and non-uniform nucleation. Notably, the UPed800 Mg-4Sn samples (Fig. 4(b, c)) exhibit no discernible defects such as dislocations, SFs, or twins in experimental observations. Consequently, all subsequent analyses regarding the dynamics of precipitate nucleation are based on uniform nucleation. Based on the classical nucleation theory (CNT), supercooling and the corresponding fluctuations in energy (ΔG*) and structure (r*) are the necessary conditions for uniform nucleation. Nearly 100 years ago, Volmer and Weber proposed the celebrated expression for the nucleation rate [54]:

$$N \propto \exp\left[-\Delta G^*/k_{\mathrm{B}}T\right] \quad (3)$$

where ΔG^* is the critical nucleation work (the barrier of nucleation) and k_{B} is the Boltzmann constant. This means that the nucleation rate N is a function of the variation in critical nucleation work ΔG^*. In addition, CNT provides an expression for the critical nucleation work

[55]:

$$\Delta G^* = 16\pi\sigma^3 T_{\mathrm{m}}^2/3(L\Delta T)^2 \quad (4)$$

where ΔT is the supercooling under atmospheric pressure. Eq. (4) shows the critical nucleation work $\Delta G^* \propto 1/\Delta T^2$. Therefore, the increase in supercooling leads to a decrease in the critical nucleation work G^*, thereby resulting in an elevation of the nucleation rate N. Experimentally, when pressure increases, the supercooling ΔT_2 of the sample can be expressed as follows:

$$\Delta T_2 = T_{\mathrm{H}} - T_0 = T_{\mathrm{m}} + \varepsilon - T_0 = \Delta T + \varepsilon \quad (5)$$

where T_{H} is the melting point and ε is the increase in melting point under high pressure, T_0 represents the ambient temperature. According to Eqs. (3) and (4), the nucleation rate of the sample with a high-pressure solid solution treatment is higher than that of the sample with an atmospheric-pressure solid solution treatment during the subsequent artificial aging process, which is attributed to an increase in supercooling induced by the variation of pressure. Furthermore, based on the CNT, an increase in supercooling also leads to a reduction in the critical nucleation radius r^* [55]. Therefore, it is reasonable to believe that the high-pressure treatment holds promising potential for enhancing the aging response from both thermodynamic and kinetic perspectives. Experimentally, the supersaturated solid solution of Mg-4Sn alloy could not be achieved by atmospheric pressure solution treatment (Fig. 2(h, i)). However, XRD data show that the UPed800 sample only contains α-Mg peak, which indicates that UP treatment can significantly improve the solid solubility limitation of Mg-Sn binary alloy. In addition, the solid solution sample reaches peak hardness in just 12 h during UPA treatment, which is an order of magnitude faster than T6 treatment under atmospheric pressure (Fig. 1(a)). Simultaneously, hardness improvement is also significantly increased from ~5 HV

under atmospheric pressure to ~20 HV. These consistent results both experimentally and theoretically confirm that the UP process can greatly enhance the aging response of Mg-Sn binary alloys. Therefore, we choose UP treatment instead of atmospheric pressure solid solution treatment.

4.2. Quick aging peak behavior during the JTed process

An external field can provide some additional parameters for tailoring the precipitation behavior of alloys. For example, electric or magnetic fields have been confirmed to effectively regulate the microstructure of Al alloys, which change the thermodynamic and kinetic conditions of phase transitions [56, 57], thereby improving or changing the microstructure, morphology, composition distribution and performance of the materials. In present work, compared to T6 and UPA treatments, the JT process achieves the shortest time (600 s) required to reach peak hardness for supersaturated solid solution UPed800 Mg-4Sn samples. This value is several orders of magnitude faster than that of previously reported aged Mg alloys (Fig. 1(a)). Basically, the formation of stable or metastable precipitates from supersaturated solid solutions is a diffusive phase transition [58]. Therefore, in addition to the necessary nucleation conditions discussed above such as supercooling and critical nucleation work, another crucial factor influencing peak hardness is the atomic diffusion rate. The atomic diffusion enhanced by the JT is generally believed to be a result of the athermal effect of electromigration besides the thermal effect [59, 60]. The net diffusion flux (j) driven by the thermal (j_t) and athermal (j_a) effects is described by the following equations [59]:

$$j = j_t + j_a = k\tau\Omega + kFN \quad (6)$$

where j_t is the diffusion flux driven by the thermal effect, j_a is the diffusion flux driven by the athermal effect, k is a constant related to the diffusion coefficient, Boltzmann constant and others, τ is the external stress, Ω is the atomic volume (cm^3/mol), N is the number of lattice atoms per unit volume (atom/cm^3), and F is the electron wind force [61]. The only force acting on the system is the electronic wind force generated by the pulse current. Thus, $\tau = F$. Consequently, the diffusion flux contributed by athermal and thermal effects depends on the values of N and Ω. The calculation results show that N (2.625×10^{22} atom/cm^3) significantly exceeds Ω (23 cm^3/mol). Namely, the diffusion flux j_a induced by the athermal effect is much larger than the diffusion flux j_t induced by the thermal effect. Experimentally, the pulse current greatly accelerates the diffusion of solute atoms, enabling the rapid formation of Mg_2Sn particles at low temperatures (below 50 °C). Similarly, the phenomenon of diffusion enhancement caused by electromigration has been reported in other alloys [62]. Therefore, compared to conventional heat treatment, the JT process holds significant potential for reaching peak hardness in Mg alloys under shorter processing time or lower temperature conditions.

4.3. The formation of nanoscale preferential-orientated precipitates

The SEM image (Fig. 2(g)) confirms that the majority of Mg_2Sn particles obviously grow in the same direction within one grain in the UPJTed Mg-4Sn alloy. As shown in the IPF maps (Fig. 5(a)), the UPJTed Mg-4Sn sample exhibits fully recrystallized grains (~356 um) and several $\{10\bar{1}2\}$ tensile twins (the interface is highlighted by solid yellow lines). Furthermore, according to the corresponding pole figures (Fig. 5(b, c)), the UPJTed sample exhibits a weak $\{10\bar{1}0\}$ texture. Note that although the weak texture leads to the Mg_2Sn particles in minority

grains being arranged in the same direction due to the basal planes of these grains having the same orientation, this does not explain that Mg_2Sn particles in one grain of the UPJTed sample only grow in a single [11$\bar{2}$0] direction instead of three [11$\bar{2}$0] directions (Fig. 3(d)). Therefore, we believe that the formation of preferential-orientated precipitates may be related to electron migration behavior. Subsequently, we establish a schematic diagram to illustrate the angles (θ_1, θ_2, and θ_3) between the electron movement direction and three [11$\bar{2}$0] directions on the basal plane (Fig. 5(d)). Experimentally, the distance between the cathode and anode remains constant. When it traverses through the crystal cell, electrons are compelled to follow a path with a minimal deflection from their original trajectory, thereby minimizing resistance along their route from the cathode to the anode [63], which aligns with Ohm's law. Evidently, among these three [11$\bar{2}$0] directions, only one exhibits the smallest angle relative to the initial electron movement direction. Consequently, the growth of Mg_2Sn phases in the UPJTed sample is restricted to a single [11$\bar{2}$0] direction in each grain.

According to Matthiessen's rule [64], intrinsic resistance is caused by electron scattering from crystal lattice vibrations. When the electrons traverse lattice planes with the lowest reticular density, they encounter minimal scattering by the crystal lattice, resulting in a path of the highest conductivity. Here, the average planar atomic density (i.e. the atomic density at the vertically projected plane of the lattice) is applied to describe the reticular density of lattice planes [63]. As depicted in Fig. 5(e–g), the planar atomic density in the [11$\bar{2}$0] orientation is found to be the lowest for Mg crystal (27.6 atoms per nm^2), indicating that electrons moving along the [11$\bar{2}$0] direction (or its equivalent) exhibit minimal resistance. Thus, the thermal and

athermal effects induced by electron migration primarily exert their influence along the $[11\bar{2}0]$ direction, providing the driving forces for the nucleation and growth of the Mg_2Sn phase.

During the traditional aging process, twelve possible ORs have been reported to exist between the Mg_2Sn phase and the α-Mg matrix [65]. While particle dimensions are different in the UPJTed Mg-4Sn alloy, only one OR: $[11\bar{2}0]_\alpha$ // $[100]_\beta$, $(0002)_\alpha$ and $(10\bar{1}0)_\alpha$ // $\{220\}_\beta$ can be confirmed for gradient Mg_2Sn particles based on the SAED patterns inserted in Fig. 3(d, i), which are obtained using a diffraction aperture with a diameter of 200 nm. According to Matthiessen's rule, the presence of low coherence interfaces (such as grain boundary or second phase interface) enhances the scattering of conducting electrons, resulting in an increment in the resistance of the alloys. In the present work, the resistance of electron movement at phase interfaces is greatly affected by atomic mismatch (δ_A) [66] and lattice mismatch (δ_L) [67]. Atomic mismatch, that is, the two planes of Mg and Mg_2Sn are overlapped in a two-dimensional coordinate system, and the mismatch between them represents the degree of scattering of electron motion by interface. Fig. 5(h) shows the schematic diagram illustrating the atomic mismatch calculations between the $(0002)_{Mg}$ and $(100)_{Mg2Sn}$ planes. The calculated results (Fig. 5(i)) reveal that the atomic and lattice mismatches between the $(220)_{Mg2Sn}$ and the basal or prismatic plane of the Mg matrix are minimal. Consequently, during the nucleation of Mg_2Sn, a parallel relationship is preferable to form between $(0002)_{Mg}$ or $(10\bar{1}0)_{Mg}$ and $(220)_{Mg2Sn}$ to ensure minimal resistance to electron movement, which is aligned with the experimental results (Figs. 3(h) and 4(h)).

4.4. The formation of refined precipitate bands

To probe the preferential nucleation phenomenon of the Mg_2Sn phase in TBs with BP facets, the DFT calculations have been performed. On the one hand, the vacancy formation energy (VE) of the Mg matrix, $\{10\bar{1}2\}$ TB and BP facet has been evaluated, respectively. The atomic models of the three structures are shown in Fig. 6(a–c). DFT results (Table 2) demonstrate that the BP facet has the lowest VE (0.606 eV), followed by TB and the matrix. Therefore, Sn atoms exhibit a preferential diffusion toward the BP facet, indicating a preferential nucleation of the Mg_2Sn phase on the BP facet. Additionally, to understand the bonding characteristics surrounding the vacancies in the Mg matrix, $\{10\bar{1}2\}$ TB and BP facet, we have calculated the electron localization function (ELF). As shown in Fig. 6(d–f), the ELF values in the vicinity of the vacancies are greater than those in other regions, suggesting significant electron localization around the vacancies. The lowest ELF value in the BP facet is related to the weakest atomic bonding, which indicates that the lower activation energies activate the diffusion of vacancies. Therefore, the Mg_2Sn phase segregation sequence is BP > TB > matrix, which is consistent with the experimental results (Fig. 4(i)), wherein the particles exhibit preferential segregation within the TB instead of in the matrix.

To further elucidate the underlying reason for the limited growth of particles in TBs, we employed an identical structural model to calculate the energy barrier for atom diffusion. Theoretically, the diffusion site with the lowest energy barrier represents the most favorable pathway for Mg_2Sn particle growth. The most probable atom diffusion paths are indicated in three structures (Fig. 7(a)), and the corresponding diffusion energy barriers are calculated (Fig. 7(b)). For pure Mg, atoms in the same layer more easily diffuse to the V2 site than to adjacent layer atoms. Comparatively, the atom diffusion mainly occurs in the TBs, which have the

lowest diffusion barrier of 0.342 eV. Evidently, the energy barriers for atom diffusion paths in TBs with BP facets exceed those of atom diffusion along smooth TBs. Accordingly, it is difficult for atoms to diffuse to the BP facet in contrast to smooth TBs. As a result, vacancies are easily formed in the BP facet for the nucleation of Mg_2Sn particles, whereas it is difficult for Mg_2Sn particles to grow rapidly due to the limited Sn diffusion in the BP facets.

To explain the formation of the refined precipitate band, the interaction between Mg_2Sn particles and TBs has been clarified by MD simulations (Fig. 8(a1–a3) and Supplementary Video 1). Compared with the freely moving TBs, the TBs with Mg_2Sn particles exhibit easy migration behaviors. Namely, coherent TBs preferentially transform into the BP facets near the particles. Simultaneously, MD simulation results demonstrate that particle segregation at the TBs reduces the stress required for initiating TB migration (Fig. 8(b)). In the deformation process, the main mode of TB migration is the transformation of coherent TBs to BP facets [68]. Owing to the particular OR of the Mg_2Sn particles (Fig. 4(a)), coupled with a minimal mismatch with Mg lattice (Fig. 5(i)), it facilitates the BP facet slip over these particles, reducing the pinning role. Therefore, TB-induced precipitation in combination with precipitate-assisted TB migration contributes to the formation of refined precipitate bands.

4.5. Strength-ductility synergy mechanisms

An abnormal strength-ductility synergy phenomenon is observed in the UPJTed Mg-4Sn alloy deformed at room temperature. The preferential-orientated gradient Mg_2Sn particles are introduced into the Mg-4Sn alloy to remarkably increase YS without scarifying ductility, relative to the UPed Mg-4Sn alloy with similar grain size (Fig. 1(b) and Table 1). To investigate the potential strength-ductility synergy mechanisms, we performed TEM

characterization of the UPJTed Mg-4Sn alloys under different strain levels. As indicated in Fig. 9(a–c), some accumulated dislocations are observed at the matrix/particle interface of coarse particles in the UPJTed Mg-4Sn alloy with a strain of 5%. The $\{10\bar{1}2\}$ extension twin initiates at this interface and propagates within the matrix. Moreover, several I_2-type SFs with an atomic arrangement of …ABABCACA… sequence, which are caused by the slipping of 1/3 $<10\bar{1}0>$ Schockley partial dislocation, are formed in the matrix. TBs act as an effective emission source for SFs, resulting in a high density of SFs within twins [69]. There is a high probability that two 1/3 $<10\bar{1}0>$ Schockley partial dislocations will interact with each other by these highly constrained twinned volume segments, and form a 1/3 $<11\bar{2}0>$ perfect dislocation [69]. Both the partial and perfect dislocations are glissile on the basal plane and thus contribute to slip on basal planes. Therefore, twinning and the subsequent SFs facilitate the deformation processes on basal planes.

Attractively, we discovered the underlying deformation mechanism within coarse Mg_2Sn particles at a medium tensile strain of 10%. Generally, deformation in aged Mg alloys at room temperature is entirely dominated by the Mg matrix owing to the differences in lattice constants and Young's moduli between the matrix and precipitates. However, as evidenced by high magnification BF-STEM images (Fig. 9(d, e)), deformation bands with dozens of atomic layers thickness are formed within the Mg_2Sn particles. The deformed structure presents two typical features. On the one hand, the HRTEM image viewed along the $[\bar{1}12]$ direction (Fig. 9(f)) reveals that the lattice structures of region I and region II are identical. It means that the coarse particle has been separated into two parts during the deformation process. The same experiment result has also been observed in Fig. 9(g) viewed along the [001] direction. On the

other hand, the shape and width of deformed bands are different, as evidenced by BF-STEM images (Fig. 9(d, e)), indicating that the coarse particle has suffered severely local plasticity shear. Furthermore, the possible shear direction is [011] according to the TEM analysis.

Since Mg_2Sn particles maintain a certain OR with Mg matrix, and the OR has a minimum mismatch, slip transmission for dislocations from the matrix into particles is possible. This hypothesis is actually confirmed by TEM observations. As deformation progresses toward the fracture strain (~15%), the particles themselves undergo both plastic deformation and shear deformation (Fig. 10(a)). An example is shown in Fig. 10(b). High-density dislocations apparently nucleate from the phase boundary and propagate into the adjacent Mg_2Sn particle at the g = (111) condition. These dislocations are likely formed to accommodate stress concentration near phase boundaries. Moreover, the local image (Fig. 10(c)) reveals that the crack is initiated from the phase boundary and subsequently propagated inward. This phenomenon deviates from the conventional crack propagation behavior observed in Mg alloys, wherein cracks usually nucleate at interfaces and propagate along them, resulting in reduced ductility [70]. In contrast, the propagation of cracks into the particles provides direct evidence to elucidate the participation of precipitates in plastic deformation. It is also confirmed by the kinking at the left side of the Mg_2Sn particle in Fig. 10(a) and the propagation of dislocations into the particle in Fig. 10(b). The high magnification BF image (Fig. 10(d)) shows the formation of a step with a height of ~20 nm at the phase boundary. As shown in the SAED pattern inserted in Fig. 10(d), the Mg_2Sn particle displays a OR of $[01\bar{1}0]_\alpha$ // $[011]_\beta$, $(0002)_\alpha$ // $(02\bar{2})_\beta$ with the surrounding Mg matrix. The HRTEM image (Fig. 10(e)) reveals the existence of a $\boldsymbol{b}$ = 1/2 [0001] partial dislocation within the matrix. A similar partial dislocation generated

by the decomposition of <*c*+*a*> dislocations has been reported in Mg alloys [69]. In addition, the Burgers vector of the partial dislocation is aligned with the shearing direction within the Mg_2Sn particle. Then, as we illustrate in Fig. 10(f), a $\boldsymbol{b}$ = 1/2 [011] full dislocation slips in parallel with the shearing direction in the sheared Mg_2Sn region. Notably, the [011] shearing direction is consistent with the analysis presented in Fig. 9. Therefore, the shearing process mainly involves two steps. Firstly, partial dislocations within the matrix slip toward the Mg_2Sn particle. Subsequently, they initiate nucleation and slipping of full dislocations within the Mg_2Sn particle, parallel to the Burgers vector of partial dislocations in the matrix. As a result, the coarse Mg_2Sn particles mainly enhance the ductility of the UPJTed Mg-4Sn alloy by undergoing plastic deformation and shear deformation themselves.

To quantitatively analyze the contributions of various strengthening mechanisms to the mechanical properties of the UPJTed Mg-4Sn alloy, the following roles have been evaluated: grain boundary strengthening, solid solution strengthening and precipitate strengthening. First of all, the flow stress of polycrystalline metals and alloys increases with decreasing grain size as formulated in the Hall-Petch relationship [71]. According to the Hall-Petch equation, the grain boundary strengthening can be evaluated approximately as 32 MPa for the UPJTed Mg-4Sn alloy. Secondly, the addition of high-concentration Sn can contribute to the strength through solution strengthening. Thus, the solution strengthening is evaluated by [72]:

$$\sigma_s = CX^{2/3} \quad (7)$$

where C is a constant that depends on the alloying element and X is the content of the solute element (4 at.%). According to the open literatures, the C for Sn is 389 MPa $(at.\%)^{-2/3}$ [73]. The solid-solution strengthening of the Sn contribution can be evaluated approximately as 46

MPa for the UPed Mg-4Sn sample. However, due to the precipitation of Mg_2Sn phases during the JT process, the contribution of solution strengthening mechanism in the UPJTed sample is even less than this value. As discussed above, the contribution of grain boundary strengthening and solid solution strengthening can be evaluated approximately as 60 MPa for UPJTed sample, which is far lower than the actual measured value (341 MPa). Therefore, we hereinafter focus on discussing the mechanism responsible for the strengthening caused by preferential-orientated gradient precipitates in the UPJTed Mg-4Sn alloy.

In general, the precipitation-strengthening is determined by the Orowan dislocation bypassing mechanism. The Orowan equation is used to estimate the strengthening effect of the nanoscale gradient precipitates [74]:

$$\sigma_{\mathrm{Orowan}} = Gb/2\pi\sqrt{1-v}(0.825\sqrt{lw/f} - 0.393l - 0.886w) \times \ln(0.866\sqrt{lw}/b) \quad (8)$$

where G is the shear modulus of the Mg matrix, l and w are the length and width of precipitates, $\boldsymbol{b}$ is the Burgers vector for dislocation, v is the Poisson ratio of Mg, f represents the volume fraction of Mg_2Sn particles. Detailed parameters are shown in Table 3. According to Eq. (8), the contribution from the Orowan strengthening by gradient Mg_2Sn particles are estimated as 255 MPa, where the contribution of coarse particles and fine particles is approximately 69 MPa and 186 MPa, respectively. Therefore, the fine Mg_2Sn particles mainly play a crucial role in strengthening. The calculated result agrees well with that of the UPJTed Mg-4Sn sample with a strain of 15% (Fig. 11(a)), wherein the distinct high-density dislocations and dislocations entanglement are observed within the refined precipitate bands. The HRTEM image (Fig. 11(b)) shows that there are obvious strain zones around fine particles. Furthermore, the corresponding

geometric phase analysis (GPA) results demonstrate a significantly higher dislocation density in the matrix than in the particles (Fig. 11(c–e)). Notably, the sum of the strengthening effect as discussed above (313 MPa) is still lower than the actual measured value (341 MPa), suggesting the existence of other strengthening mechanisms contributing to the strength.

The dislocation-shearing mechanism may be activated when the precipitates have good coherence with the matrix [75]. In the present work, the interface relationship of the preferential-orientated gradient Mg_2Sn particles satisfies the criteria, which provides favorable conditions for the dislocation-shearing mechanism. Experimentally, shear deformation of coarse particles has been observed in Fig. 10(d). The increment in YS through the dislocation-shearing mechanism of coarse particles can mainly be contributed by coherent strengthening ($\Delta\sigma_{CS}$) [76]. Based on the discussion abovementioned, a high-density fine Mg_2Sn particles are the groundwork for achieving an excellent tensile strength in the UPJTed Mg-4Sn alloys at room temperature. In addition, the coarse particles can mediate dislocation glide and alleviate stress concentration in terms of shear deformation, leading to a good combination of strength and ductility.

5. Conclusions

In summary, the unique preferentially-orientated gradient Mg_2Sn particles segregation phenomenon, formation reason and strength-ductility synergy mechanism in the UPJTed Mg-4Sn (at.%) alloys are elucidated by HRTEM observations, DFT calculations and MD simulations. The following conclusions can be drawn:

(1) A unique preferentially-orientated gradient structure has been first achieved by performing a novel UPJTed process, wherein the average size of coarse particles and fine particles in the Mg-4Sn alloy is approximately 216 nm and 33.8 nm respectively. Moreover, both coarse and fine particles exhibit identical ORs: $[11\bar{2}0]_{\alpha} \,||\, [100]_{Mg_2Sn}$, $(0002)_{\alpha}$ and $[10\bar{1}0]_{\alpha} \,||\, \{220\}_{Mg_2Sn}$ owing to the movement of electrons along the path of minimal scattering by the crystal lattice.

(2) Both high YS (341 ± 9.6 MPa) and good EL (15% ± 1 %) of the UPJTed Mg-4Sn alloys are simultaneously attained at room temperature, which exceeds the majority of the Mg-Sn and conventional T6-state Mg-RE based alloys reported thus far. Attractively, the JTed technique, which only requires 600 s to reach peak hardness, is the most time-efficient aging method for aged Mg alloys.

(3) According to DFT calculations, the trend of Sn atom segregation is in the following order: BP facet > $\{10\bar{1}2\}$ TB > Mg matrix. Meanwhile, the theoretical results reveal that the nucleation of Mg_2Sn particles can occur easily in BP facets, but the growth of these particles is greatly prohibited. Moreover, MD simulation results demonstrate that particle segregation at TBs reduces the critical stress to initiate TB migration due to its unique OR. Hence, TB-induced precipitation in combination with precipitate-assisted TB migration contributes to the formation of refined precipitate bands.

(4) The experimental results confirm that the strengthening role is mainly associated with the presence of gradient Mg_2Sn particles, especially fine particles can significantly pin dislocations and induce Orowan strengthening. In contrast, the enhanced ductility is

attributed to the coarse Mg_2Sn particles, which can undergo plastic/shear deformation associated with the activation of 1/2 [011] full dislocations.

Acknowledgments

This work is financially supported by National Science Foundation of China (Nos. 52331033, 52171126 and 52202374) and the Natural Science Foundation of Hebei Province (Nos. E2022203167, E2023203255 and 236Z1020G) and Innovation Groups Program (No. C2022203003). We would like to express our gratitude to the Ministry of Education Yangtze River Scholar Professor Program (No. T2020124). We also thanked Prof. Yunchang Xin's group for the related EBSD measurements.

References

[1] T. Trang, J. Zhang, J. Kim, A. Zargaran, J. Hwang, B. Suh, N. Kim, Nat. Commun. 9 (2018) 2522.

[2] Z. Wu, R. Ahmad, B. Yin, S. Stefanie, W. Curtin, Science 359 (2018) 447-452.

[3] G. Wu, K. Chan, L. Zhu, L. Sun, J. Lu, Nature 545 (2017) 80-83.

[4] S. Tang, T. Xin, W. Xu, D. Miskovic, G. Sha, Z. Quadir, S. Ringer, K. Nomoto, N. Birbilis, M. Ferry, Nat. Commun. 10 (2019) 1003.

[5] L. Chen, J. Xu, H. Choi, M. Pozuelo, X. Ma, S. Bhowmick, J. Yang, S. Mathaudhu, X. Li, Nature 528 (2015) 539-543.

[6] M. Yoo, J. Lee, Philos. Mag. A 63 (1991) 987-1000.

[7] M. Yoo, Metall. Mater. Trans. A 12 (1981) 409-418.

[8] C. Yan, Y. Xin, X. Chen, D. Xu, P. Chu, C. Liu, B. Guan, X. Huang, Q. Liu, Nat. Commun. 12 (2021) 4616.

[9] Y. Cui, Y. Li, Z. Wang, Q. Lei, Y. Koizumi, A. Chiba, Int. J. Plast. 99 (2017) 1-18.

[10] F. Mouhib, Z. Xie, A. Atila, J. Guénolé, S. KorteKerzel, T. Al-Samman, Acta Mater. 266 (2024) 119677.

[11] W. Woo, H. Choo, M. Prime, Z. Feng, B. Clausen, Acta Mater. 56 (2008) 1701-1711.

[12] S. Jiang, H. Wang, Y. Wu, X. Liu, H. Chen, M. Yao, B. Gault, D. Ponge, D. Raabe, A. Hirata, M. Chen, Y. Wang, Z. Lu, Nature 544 (2017) 460-464.

[13] C. Liu, Y. Hu, Y. Liu, H. Tseng, T. Huang, C. Lu, Y. Chuang, S. Cheng, Acta Mater. 61 (2013) 5713-5719.

[14] F. Elsayed, T. Sasaki, C. Mendis, T. Ohkubo, K. Hono, Scr. Mater. 68 (2013) 797-800.

[15] Q. Wang, J. Chen, Z. Zhao, S. He, Mater. Sci. Eng. A 528 (2010) 323-328.

[16] T. Homma, N. Kunito, S. Kamado, Scr. Mater. 61 (2009) 644-647.

[17] H. Fu, B. Ge, Y. Xin, R. Wu, C. Fernandez, J. Huang, Q. Peng, Nano Lett. 17 (2017) 6117-6124.

[18] Q. Peng, Y. Sun, B. Ge, H. Fu, Q. Zu, X. Tang, J. Huang, Acta Mater. 169 (2019) 36-44.

[19] H. Fu, Q. Peng, J. Guo, B. Liu, W. Wu, Scr. Mater. 76 (2014) 33-36.

[20] B. Ge, H. Fu, K. Deng, Q. Zhang, Q. Peng, Bioact. Mater. 3 (2018) 250-254.

[21] G. Kresse, J. Hafner, Phys. Rev. B 47 (1993) 558.

[22] G. Kresse, D. Joubert, Phys. Rev. B 59 (1999) 1758-1775.

[23] J. Perdew, K. Burke, M. Ernzerhof, Phys. Rev. Lett. 77 (1996) 3865-3868.

[24] J. Perdew, K. Burke, Y. Wang, Phys. Rev. B 54 (1996) 16533-16539.

[25] K. Momma, F. Izumi, J. Appl. Crystallogr. 41 (2008) 653-658.

[26] Y. Kim, N. Kim, B. Lee, Calphad 33 (2009) 650-657.

[27] E. Baibuz, S. Vigonski, J. Lahtinen, J. Zhao, V. Jansson, V. Zadin, F. Djurabekova, Comput. Mater. Sci. 146 (2018) 287-302.

[28] K. Kim, J. Jeon, B. Lee, Calphad 48 (2015) 27-34.

[29] J. Honeycutt, H. Andersen, J. Phys. Chem. 91 (1987) 4950-4963.

[30] A. Stukowski, Model. Simul. Mater. Sci. Eng. 18 (2009) 015012.

[31] K. Wang, X. Wang, C. Dang, S. Wang, S. Huang, M. Liu, J. Wang, J. Mater. Res. Technol. 25 (2023) 7169-7179.

[32] K. Liu, L. Rokhlin, F. Elkin, D. Tang, J. Meng, Mater. Sci. Eng. A 527 (2010) 828-834.

[33] J. Li, Z. He, P. Fu, Y. Wu, L. Peng, W. Ding, Mater. Sci. Eng. A 651 (2016) 745-752.

[34] J. Jiang, L. Tong, Z. Xu, G. Bi, C. Cao, Y. Li, T. Chen, W. Fu, D, J. Mater. Res. Technol. 23 (2023) 2601-2611.

[35] Z. Ma, G. Li, Q. Peng, X. Peng, D. Chen, H. Zhang, Y. Yang, G. Wei, W. Xie, J. Magnes. Alloys 10 (2022) 119-128.

[36] Z. Shi, J. Xu, J. Yu, X. Liu, Mater. Sci. Eng. A 712 (2018) 65-72.

[37] Y. Liu, Z. Zhang, J. Wang, Y. Li, H. Li, L. Jia, J. Wang, J. Zhang, J. Magnes. Alloys 11 (2023) 720-734.

[38] L. Zhong, Y. Wang, Y. Dou, J. Magnes. Alloys 7 (2019) 637-647.

[39] Y. Li, A. Zhang, C. Li, H. Xie, B. Jiang, Z. Dong, P. Jin, F. Pan, J. Mater. Res. Technol. 26 (2023) 2919-2940.

[40] J. Zhang, S. Liu, R. Wu, L. Hou, M. Zhang, J. Magnes. Alloys 6 (2018) 277-291.

[41] X. Zhuo, L. Zhao, W. Gao, Y. Wu, H. Liu, P. Zhang, Z. Hu, J. Jiang, A. Ma, J. Mater. Res. Technol. 21 (2022) 186-211.

[42] T. Sasaki, F. Elsayed, T. Nakata, T. Ohkubo, S. Kamado, K. Hono, Acta Mater. 99 (2015) 176-186.

[43] A. De Luca, D. Seidman, D. Dunand, Acta Mater. 165 (2019) 1-14.

[44] S. Yin, C. Chen, X. Yan, X. Feng, R. Jenkins, P. O'Reilly, M. Liu, H. Li, R. Lupoi, Addit. Manuf. 22 (2018) 592-600.

[45] A. De Luca, D. Dunand, D. Seidman, Acta Mater. 119 (2016) 35-42.

[46] K. Yang, Y. Wang, M. Guo, H. Wang, Y. Mo, X. Dong, H. Lou, Prog. Mater. Sci. 138 (2023) 101141.

[47] A. Kwiatkowski da Silva, I. Souza Filho, W. Lu, K. Zilnyk, M. Hupalo, L. Alves, D. Ponge, B. Gault, D. Raabe, Nat. Commun. 13 (2022) 2330.

[48] Q. Peng, W. Wu, J. Guo, J. Xiang, S. Zhao, J. Appl. Phys. 115 (2014) 023511.

[49] C. Shu, C. Liang, K. Lin, Mater. Sci. Eng. A 772 (2020) 138689.

[50] Y. Liao, C. Chen, C. Liang, K. Lin, A.T. Wu, Acta Mater. 200 (2020) 200-210.

[51] J. Nie, Y. Zhu, J. Liu, X. Fang, Science 340 (2013) 957-960.

[52] H. Huang, T. Lin, Q. Fu, L. Chen, K. Chen, Q. Hou, C. Li, G. Wen, Ceram. Int. 48 (2022) 18784-18792.

[53] Y.S. Han, H.I. Lee, D.H. Kim, Y.G. Kim, Scr. Metall. Mater. 31 (1994) 1623-1628.

[54] M. Volmer, A. Weber, Z. Phys. Chem. 119 (1926) 277-301.

[55] M. Perez, M. Dumont, D. Acevedo-Reyes, Acta Mater. 56 (2008) 2119-2132.

[56] J. Luo, H. Luo, C. Liu, T. Zhao, R. Wang, Y. Ma, Mater. Sci. Eng. A 798 (2020) 139990.

[57] Y. Wang, Y. Zhao, X. Xu, D. Pan, W. Jiang, X. Yang, Z. Wang, Mater. Sci. Eng. A 735 (2018) 154-161.

[58] Q. Luo, Y. Guo, B. Liu, Y. Feng, J. Zhang, Q. Li, K. Chou, J. Mater. Sci. Technol. 44 (2020) 171-190.

[59] R. Zhu, Y. Jiang, L. Guan, H. Li, G. Tang, J. Alloys Compd. 658 (2016) 548-554.

[60] G. Hu, Y. Zhu, G. Tang, C. Shek, J. Liu, J. Mater. Sci. Technol. 27 (2011) 1034-1038.

[61] J. Lloyd, J. Phys. D, Appl. Phys. 32 (1999) R109-R118.

[62] X. Huang, L. Yan, X. Zhang, Scr. Mater. 202 (2021) 114017.

[63] S. Deng, R. Li, T. Yuan, P. Yang, S. Xie, J. Li, Appl. Phys. Lett. 117 (2020) 194102.

[64] A. Matthiessen, G. Vogt, Ann. Phys. 122 (1864) 19-31.

[65] H. Chen, Z. Shi, Mater. Lett. 281 (2020) 128648.

[66] B. Bramfitt, Metall. Trans. 1 (1970) 1987-1995.

[67] M. Zhang, P. Kelly, M. Qian, J. Taylor, Acta Mater. 53 (2005) 3261-3270.

[68] K. Xie, K. Hazeli, N. Dixit, L. Ma, K. Ramesh, K. Hemker, Sci. Adv. 7 (2021) eabg3443.

[69] S. Zhu, S. Ringer, Acta Mater. 144 (2018) 365-375.

[70] A. Srinivasan, J. Swaminathan, M. Gunjan, U. Pillai, B. Pai, Mater. Sci. Eng. A 527 (2010) 1395-1403.

[71] H. Yu, C. Li, Y. Xin, A. Chapuis, X. Huang, Q. Liu, Acta Mater. 128 (2017) 313-326.

[72] M. Fan, Y. Cui, Y. Zhang, X. Wei, X. Cao, P.K. Liaw, Y. Yang, Z. Zhang, J. Magnes. Alloys 11 (2023) 1321-1331.

[73] B. Shi, R. Chen, W. Ke, J. Alloys Compd. 509 (2011) 3357-3362.

[74] J. Nie, Scr. Mater. 48 (2003) 1009-1015.

[75] K. Ming, X. Bi, J. Wang, Int. J. Plast. 100 (2018) 177-191.

[76] L. Liu, Y. Zhang, J. Li, M. Fan, X. Wang, G. Wu, Z. Yang, J. Luan, Z. Jiao, C.T. Liu, Int. J. Plast. 153 (2022) 103235.

[77] X. Qi, Y. Li, X. Xu, Y. Liu, H. Zhang, Q. Zhu, G. Zhu, J. Wang, M. Huang, X. Zeng, J. Mater. Sci. Technol. 166 (2023) 123-132.

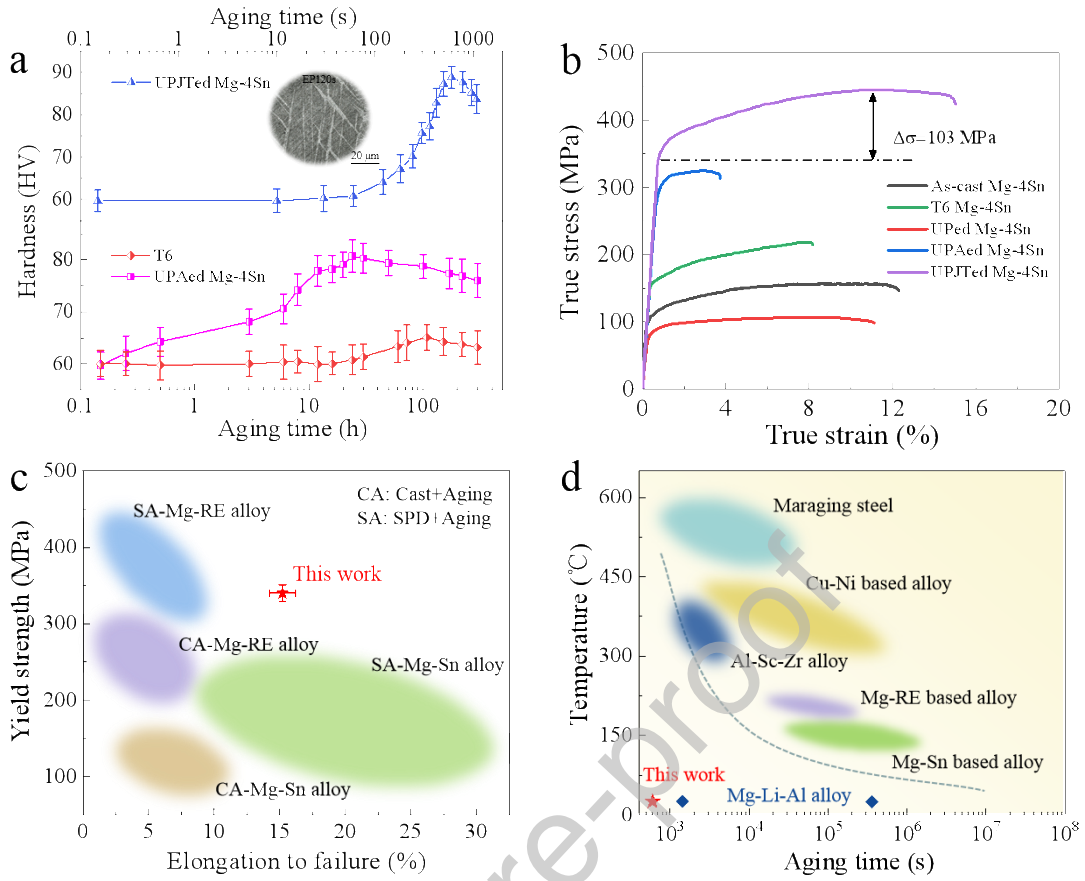

Fig. 1. Mechanical properties of Mg-4Sn alloys. (a) The aging response curves of the Mg-4Sn alloys under different aging conditions. (b) Ture stress-strain curves of Mg-4Sn alloys with different states. (c) Comparison of YS and EL of various Mg-Sn-based and Mg-RE-based aging alloys by different fabrication techniques. (d) Comparison of the aging response of various alloys.

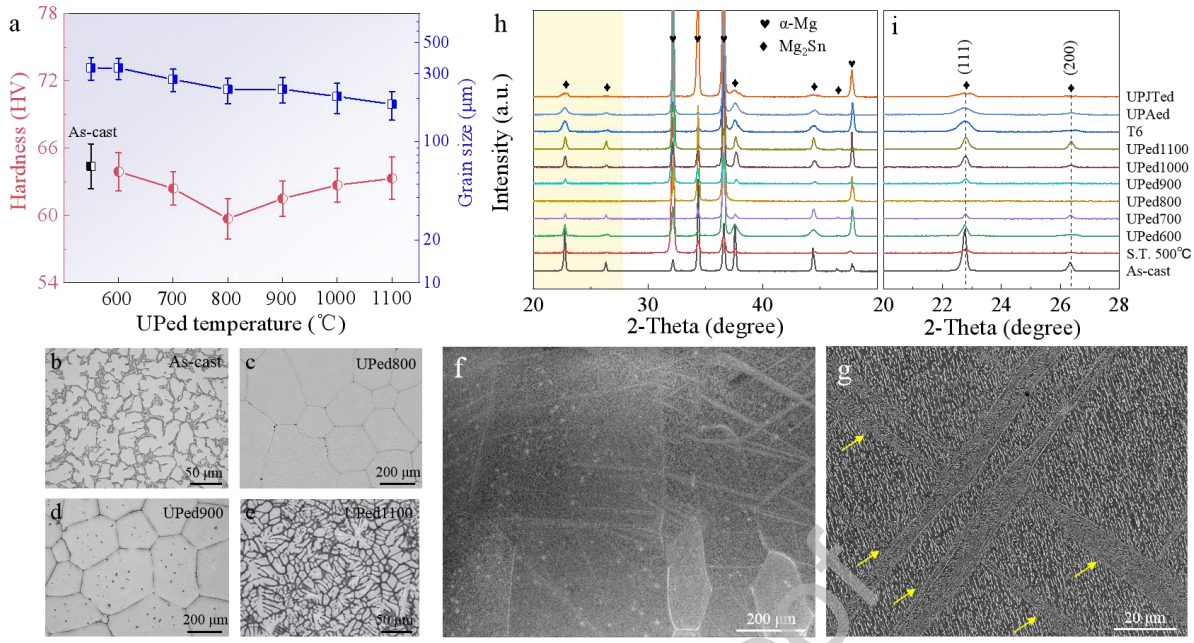

Fig. 2. Hardness variation and microstructure characteristics of Mg-4Sn samples. (a) Microhardness and grain size variation of Mg-4Sn alloys prepared under different UPed temperatures. (b–e) Typical optical structures under different UPed temperature. (f, g) Local low and high resolution SEM image of the UPJTed Mg-4Sn alloys. (h) XRD full patterns of Mg-4Sn alloy under different conditions measured at room temperature. (i) Expanded patterns for details ranging from 20° to 28°.

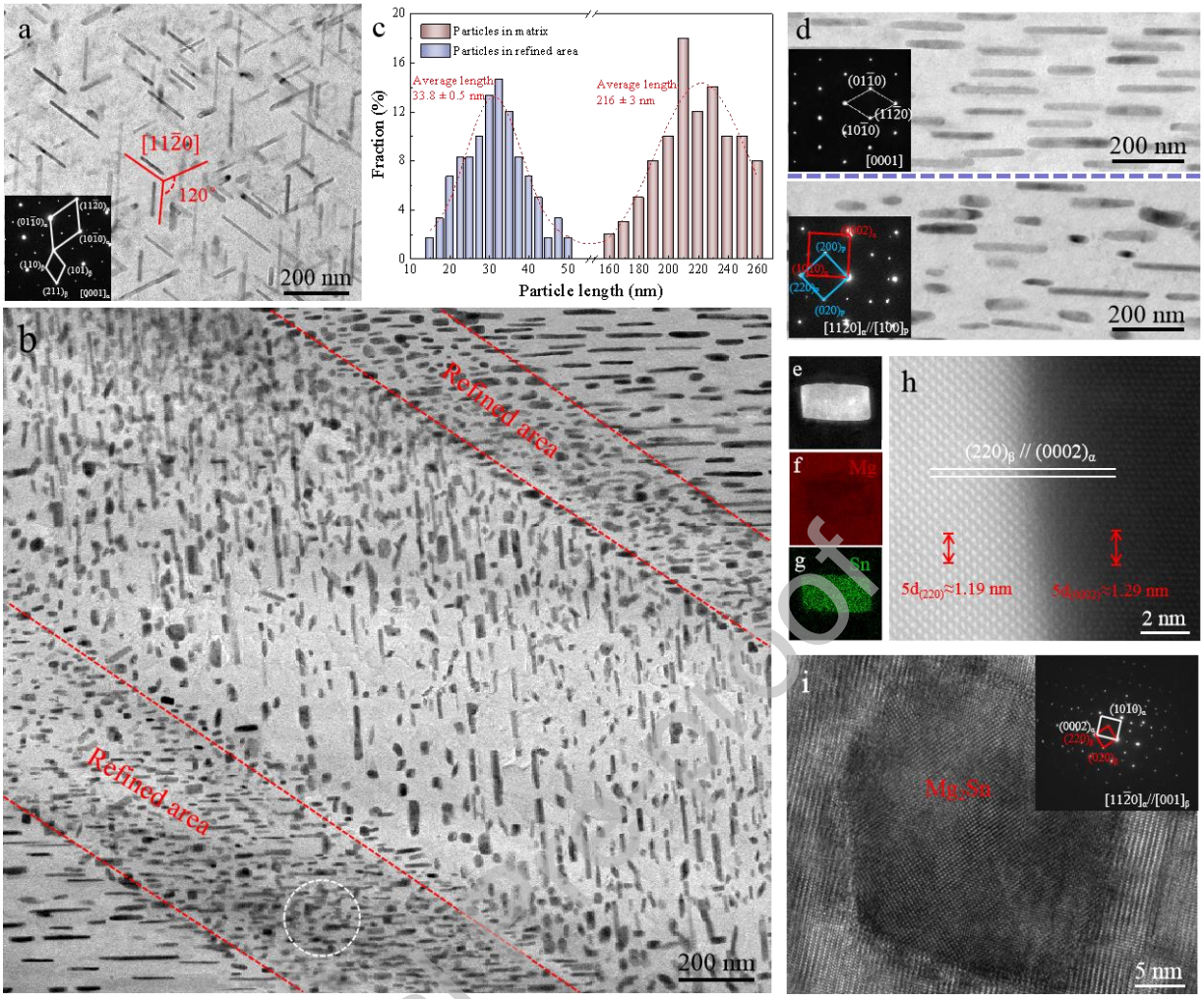

Fig. 3. Microstructure characteristics of the UPJTed Mg-4Sn alloy. (a, b) Bright-field TEM images of the UPAed and UPJTed samples, respectively. (c) Average length of Mg_2Sn particles in the UPJTed sample. The average size of coarse and fine particles was calculated based on 100 random dots. (d) High-magnification BF images showing precipitates in the UPJTed sample. The inset shows the SAED patterns of the matrix indexed along [0001] and [11$\bar{2}$0] directions. (e–g) the corresponding EDS analysis of Mg_2Sn particles in the UPJTed sample. (h) The atomic-level interface between matrix and Mg_2Sn in the UPJTed sample. (i) HRTEM image of Mg_2Sn particles in refined area. The inset is the SAED pattern.

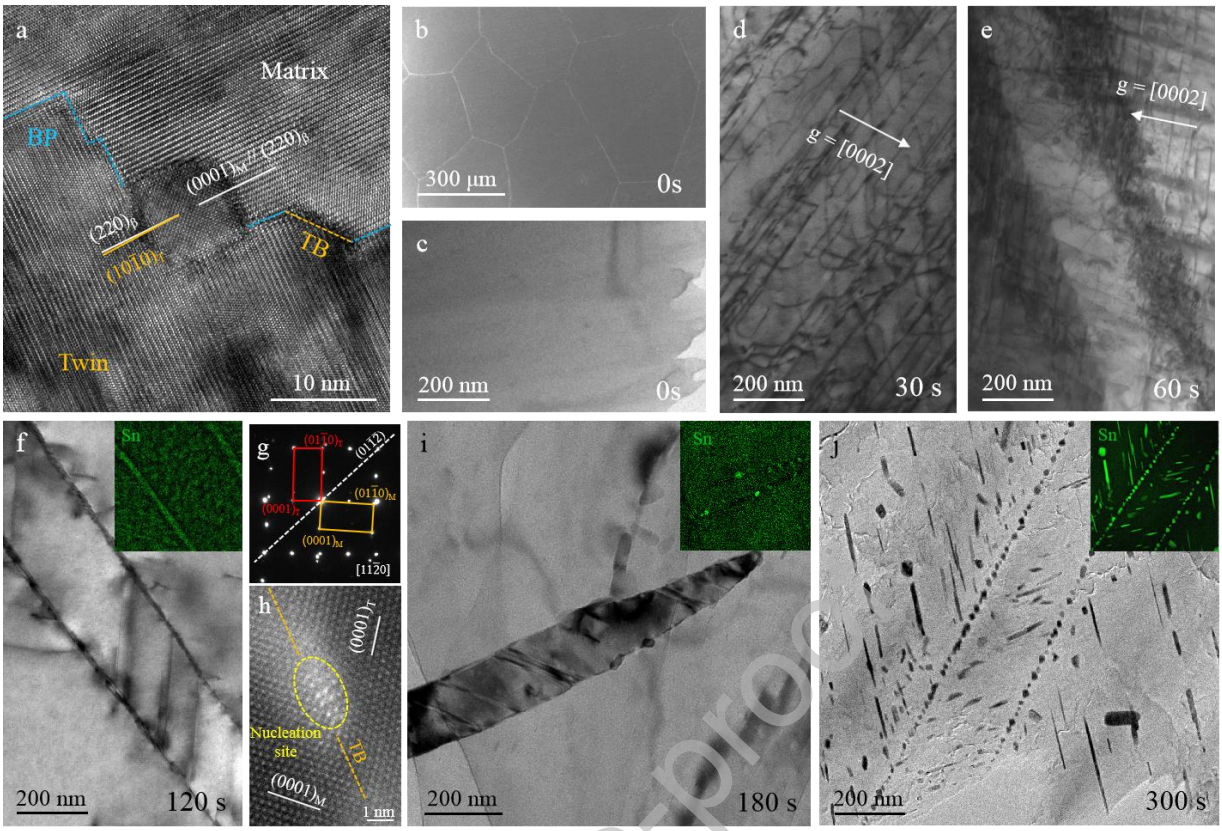

Fig. 4. Microstructural evolution of TBs during the JT. (a) HRTEM image of the UPJTed sample showing the Mg_2Sn particles in the $\{10\bar{1}2\}$ TB viewed in the $[11\bar{2}0]_{Mg}$. (b) Low magnification SEM image of the UPed800 Mg-4Sn alloy. (c–j) BF images of Mg matrix under electric current stress as a function of time in the UPed800 sample. The insets exhibit the corresponding EDS mapping, indicating Sn atom segregation and Mg_2Sn nucleation in TBs. (d, e) are obtained under the two-beam condition of g = (0002). (f–j) are obtained with the electron beam parallel to $[11\bar{2}0]$. (g, h) The corresponding SAED pattern and high-resolution HAADF-STEM image of (f).

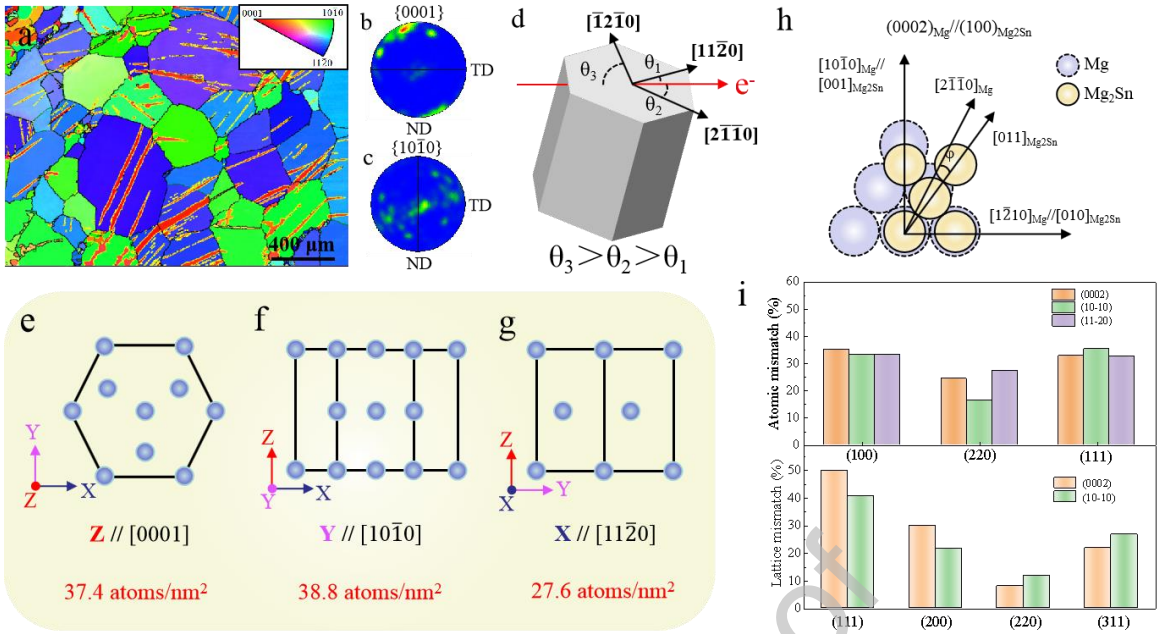

Fig. 5. Preferentially-orientated precipitates (a) Inverse pole figure maps of UPJTed Mg-4Sn alloys. (b, c) (0001) and (10$\bar{1}$0) pole figures were analyzed from (a), respectively. (d) Schematic diagram of the angle between the electron motion direction in the Mg matrix and three [11$\bar{2}$0] directions on the basal plane. Projected images of Mg unit cell along (e) [0001], (f) [10$\bar{1}$0] and (g) [11$\bar{2}$0] directions, respectively. (h) Crystallographic relationships between Mg and Mg_2Sn for atomic mismatch calculations. (i) The histogram of lattice mismatch and atomic mismatch, which was calculated between the basal or prismatic planes of the Mg matrix and some low-index planes of the Mg_2Sn particle.

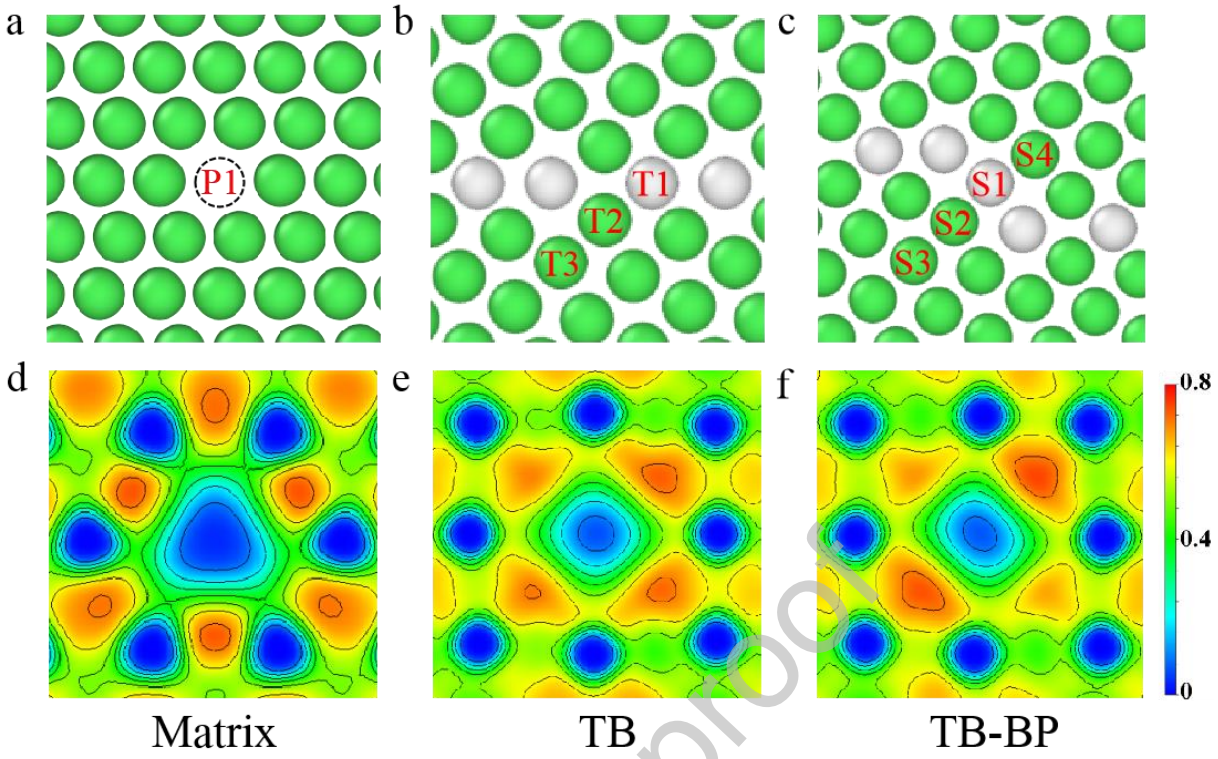

Fig. 6. Vacancy formation energy and ELF calculations. Vacancy structures in (a) pure Mg, (b) $\{10\bar{1}2\}$S TB and (c) $\{10\bar{1}2\}$ TB-BP interface, respectively. The electron localization functions for vacancy models in (d) pure Mg, (e) $\{10\bar{1}2\}$ TB and (f) $\{10\bar{1}2\}$ TB-BP interface, respectively.

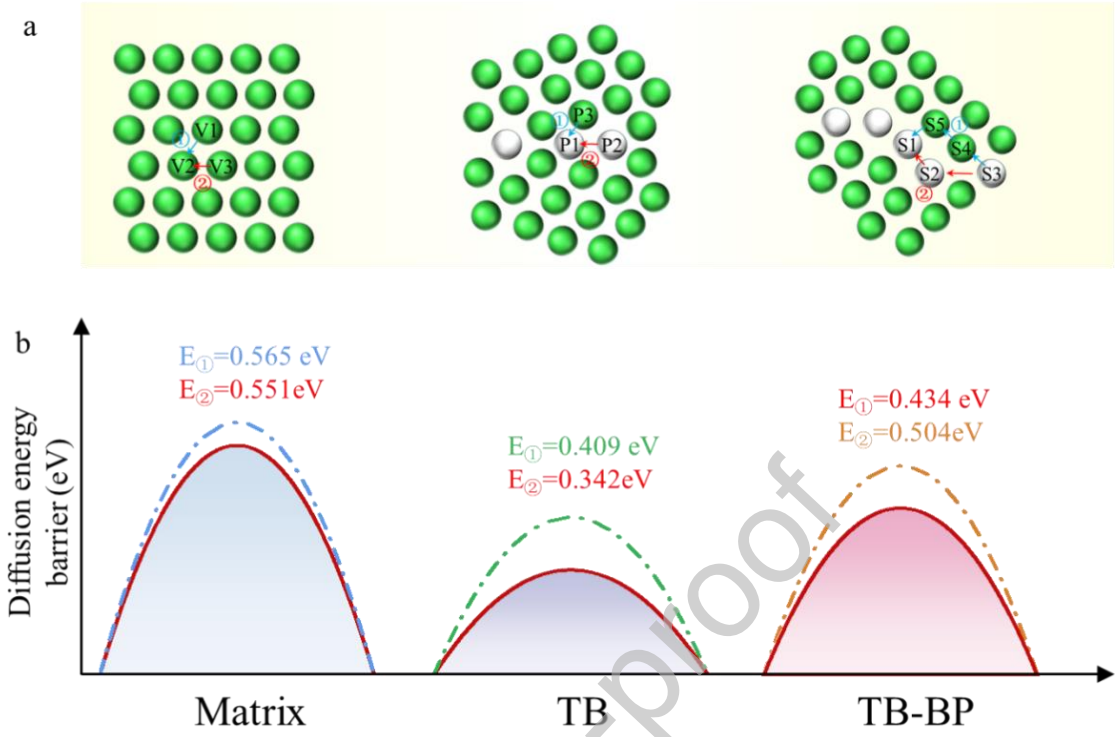

Fig. 7. Diffusion energy barrier calculations. (a) Diffusion paths from surrounding sites to vacancy sites in three different states of pure Mg, $\{10\bar{1}2\}$ TB and $\{10\bar{1}2\}$ TB-BP interface. (b) Diffusion energy barriers of different diffusion paths in three different states.

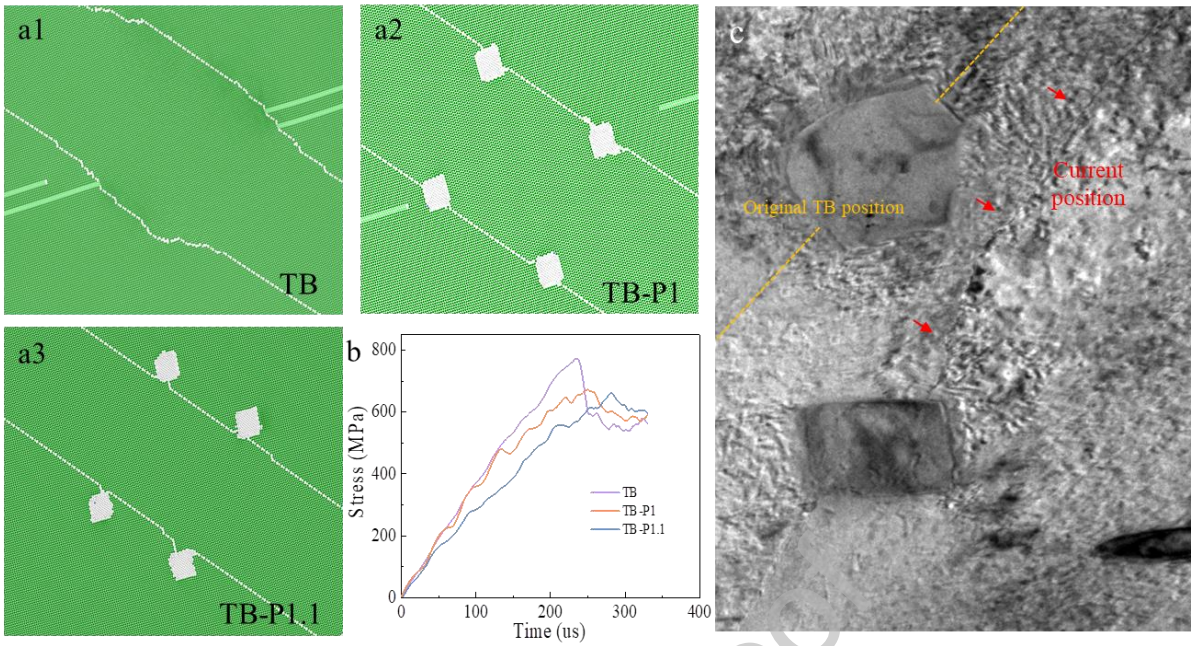

Fig. 8. Interactive roles between Mg_2Sn and $\{10\bar{1}2\}$ twin. Movement processes of twin boundaries (captured from Video 1), (a1) pure $\{10\bar{1}2\}$ TB, (a2) two particles segregated on $\{10\bar{1}2\}$ TB, (a3) two particles segregated in front of $\{10\bar{1}2\}$ TB. (b) Stress-time relationship of the different TB movements. (c) Week pinning role of Mg_2Sn particle on TB slip.

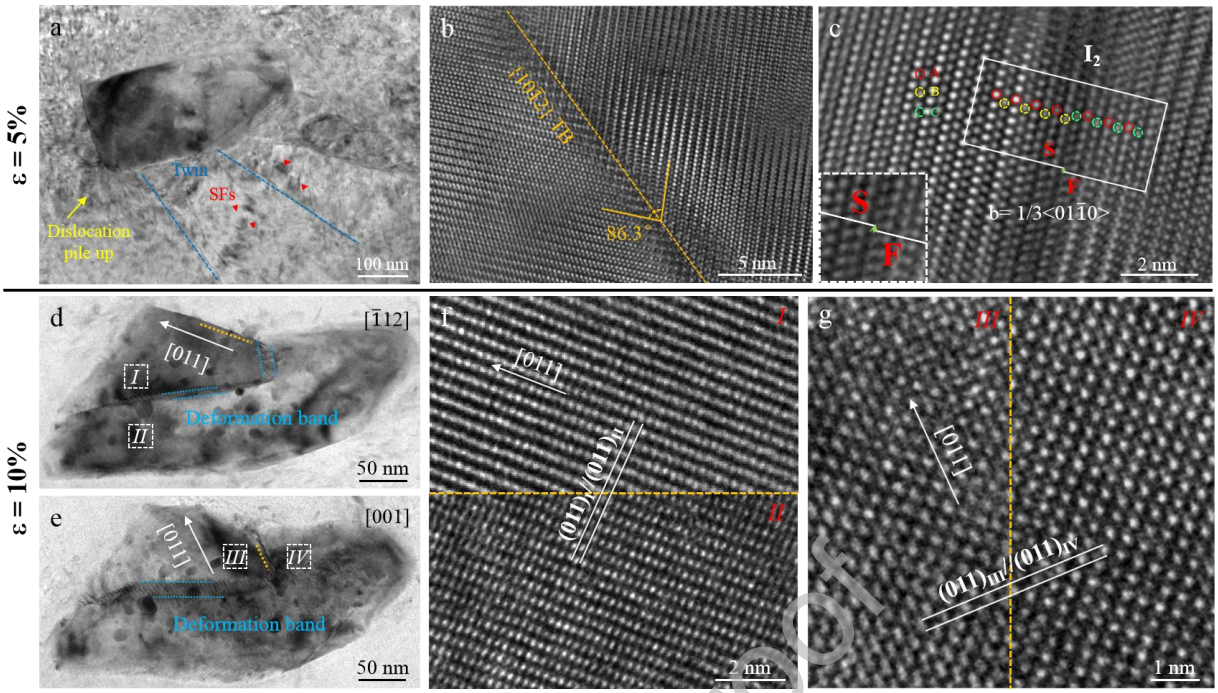

Fig. 9. Deformation behavior of the coarse Mg_2Sn particles in the deformed UPJTed Mg-4Sn alloy. (a) TEM images of coarse Mg_2Sn particles with a strain of 5%. HRTEM images of TB (b) and SFs (c) in Mg matrix. S and F indicate the starting and ending points of a Burgers circuit, respectively. Green arrows near S and F reveal the Burgers vector direction. (d, e) BF image of locally sheared coarse particles with a strain of 10% along the [$\bar{1}$12] and [001] zone axis, respectively. (f, g) HRTEM images of the lattice structure in sheared and unsheared regions corresponding to (d) and (e), respectively.

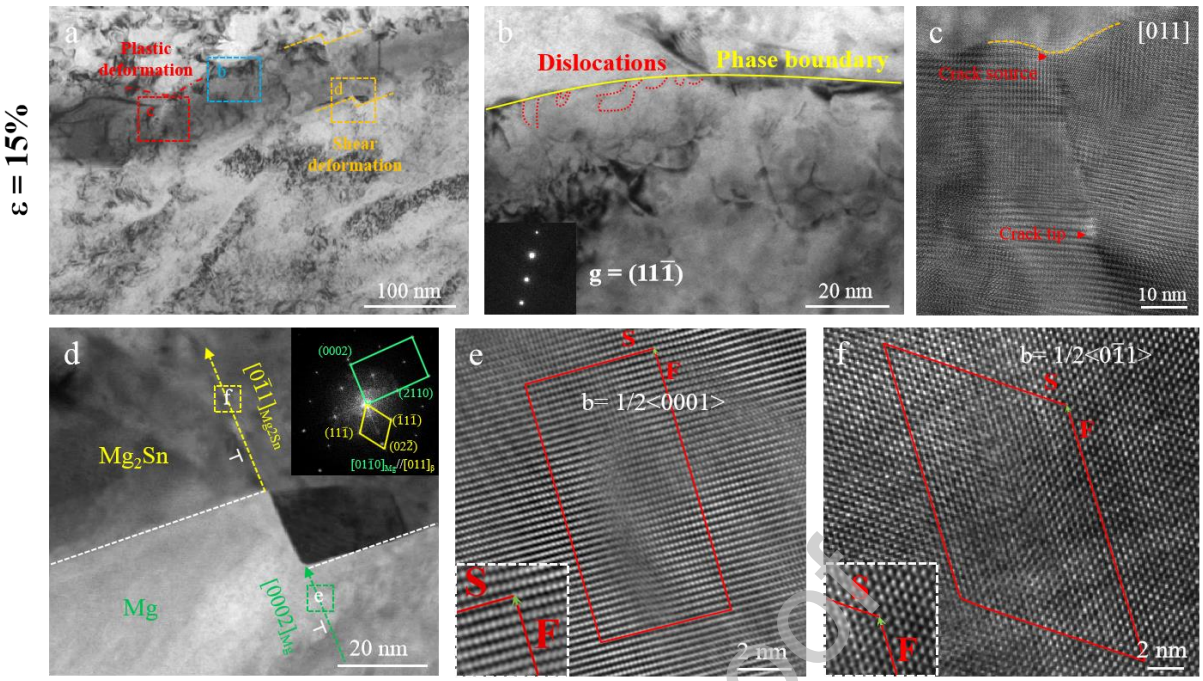

Fig. 10. Shear deformation behavior of the coarse Mg_2Sn particles in the deformed UPJTed Mg-4Sn alloy. (a) TEM images of coarse Mg_2Sn particles with a strain of 15%. (b) Two-beam BF image taken along the [011] zone axis under g = (111) condition of blue dotted box inserted in (a). (c) HRTEM image of red dotted box inserted in (a). (d) High magnification HAADF-STEM image of the interface between Mg matrix and sheared Mg_2Sn particle marked orange dashed box in (a). Corresponding SAED pattern of the sheared Mg_2Sn particle and Mg matrix along the $[01\bar{1}0]_{\alpha}$ zone axis inserted in the right corner. (e, f) The HRTEM image reveals $\boldsymbol{b}$ = 1/2 [0001] partial dislocation and $\boldsymbol{b}$ = 1/2 [011] full dislocation in the Mg matrix and sheared Mg_2Sn particle, respectively.

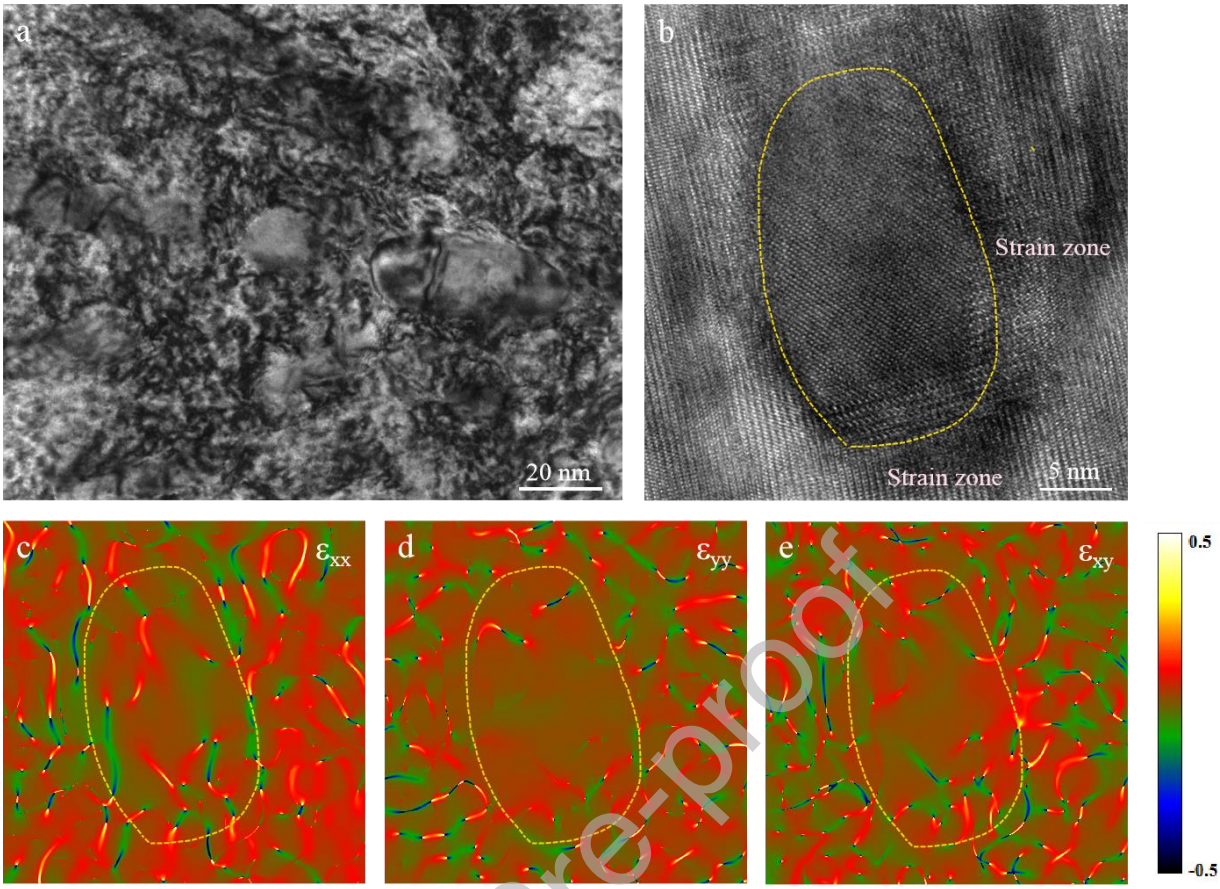

Fig. 11. Microstructural characteristics of the fine Mg_2Sn particles in the deformed UPJTed Mg-4Sn alloy (ε =15%, ε represents strain). (a) High magnification BF image of refined precipitate bands in UPJTed Mg-4Sn alloy. (b) HRTEM image of fine Mg_2Sn particle after a strain of 15%. (c–e) The GPA analysis of the fine Mg_2Sn particle in (b).

Table 1 Tensile properties of the Mg-4Sn samples under different conditions.

Sample	YS (MPa)	UTS (MPa)	EL (%)
As-cast	94.7 ± 3.7	155.3 ± 6.2	12.3 ± 1
T6	151.2 ± 4.7	218.2 ± 6.9	8.2 ± 0.4
UPed	83.2 ± 4.3	106.5 ± 7.4	11.1 ± 0.8
UPAed	290.4 ± 7.7	324.3 ± 7.2	3.7 ± 0.3
UPJTed	341.1 ± 9.6	444.6 ± 12.1	15 ± 1

(YS: yield strength; UTS: ultimate tensile strength; EL: elongation to fracture)

Table 2 The calculation results of vacancy formation energy was performed by DFT. The standard deviation is 0.01.

Vacancy site (VE)	Vacancy formation energy (eV)
VE_{P1}	0.883
VE_{T1}	0.699
VE_{T2}	0.812
VE_{T3}	0.845
VE_{S1}	0.606
VE_{S2}	0.727
VE_{S3}	0.866
VE_{S4}	0.764

Table 3 Detailed parameters for solution strengthening and precipitation strengthening.

Parameters	Values
C	389 MPa (at.%)$^{-2/3}$ [73]
X	4 at.%
G	16.6 GPa [77]
b	0.32 nm [77]
v	0.32 [77]
l_{coarse}	216 nm
w_{coarse}	70 nm
l_{fine}	33.8 nm
w_{fine}	28.5 nm

Graphical abstract

We firstly report a unique preferentially-orientated double-scale structure achieved by applying an ultrahigh-pressure treatment that is followed by Joule heat treatment. The formation reason and strength-ductility synergistic mechanism have been elucidated by HRTEM observations, DFT calculations and MD simulations. The finding might provide some implications for precipitation engineering to tune the mechanical properties of metals.

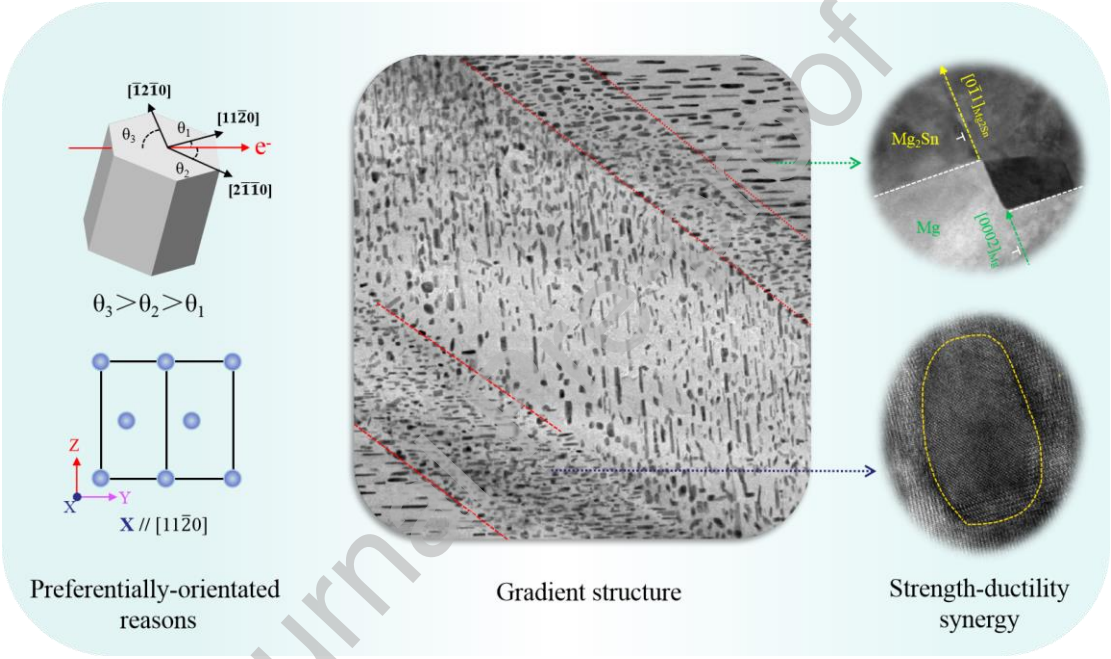

Declaration of interests

☒ The authors declare that they have no known competing financial interests or personal relationships that could have appeared to influence the work reported in this paper.

☐ The author is an Editorial Board Member/Editor-in-Chief/Associate Editor/Guest Editor for *[Journal name]* and was not involved in the editorial review or the decision to publish this article.

☐ The authors declare the following financial interests/personal relationships which may be considered as potential competing interests: